WILEY

RESEARCH ARTICLE OPEN ACCESS

Complex High-Cyclic Loading in an Accumulation Model for Sand

Patrick Staubach[1] | Lukas Knittel[2] | Torsten Wichtmann[3]

[1]Chair of Geotechnics, Institute of Structural Engineering, Bauhaus-University Weimar, Weimar, Germany | [2]Keller Grundbau GmbH, Renchen, Germany | Institute of Soil Mechanics and Rock Mechanics, Karlsruhe Institute of Technology, Karlsruhe, Germany | [3]Chair of Soil Mechanics, Foundation Engineering and Environmental Geotechnics, Ruhr-University Bochum, Bochum, Germany

Correspondence: Patrick Staubach (patrick.staubach@uni-weimar.de)

ABSTRACT

Experimental evidence indicates that multidimensional cyclic loading of soils causes larger accumulation of deformations than equivalent one-dimensional loading. The response of sand to high-cyclic loading with 10,000 cycles and up to four-dimensional stress paths (i.e., four independent oscillating components) is examined in 120 triaxial and hollow cylinder tests in this work to extend these findings. With increasing number of oscillating stress components, the accumulation of permanent strains tends to increase. It is demonstrated that the definition of the multidimensional strain amplitude incorporated in the high-cycle accumulation (HCA) model can account for this. The validation of the HCA model for complex cyclic loading is complemented by the simulation of model tests on monopile foundations of offshore wind turbines subjected to multidirectional cyclic loading, for which the consideration of spatially variable cyclic loading with nonconstant load amplitudes in the HCA model is discussed. For this purpose, an extension of the HCA model considering multiple strain amplitudes is presented.

1 | Introduction

Traffic (such as high-speed trains and magnetic levitation trains [1]), industrial sources (such as crane rails and machine foundations [2, 3]), wind and waves (such as on- and offshore wind turbines and coastal structures [4]), repeatedly filling and emptying processes (such as locks, tanks, and silos [5]), construction processes (such as pile installation by vibration [6]), or granular soil compaction (such as vibratory compaction [7]) can all result in a high-cyclic loading of soils. A comparatively high number of cycles ($N \gtrsim 10^3$) and relatively low strain amplitudes ($\varepsilon^{\mathrm{ampl}} \lesssim 10^{-3}$) are characteristics of this loading. High-cyclic loading may cause a buildup of persistent deformations and/or stress changes in the soil, depending on the boundary conditions. The serviceability of a foundation can be compromised by excessively accumulated deformations, particularly differential settling with associated skewing. For example, the turbines of a wind power plant tolerate only small amounts of skew. In the case of high-speed railway tracks, very small settlement differences must also be guaranteed. Sometimes excessive accumulated settlements in real structures are reported, for example in Refs. [8–12]. The expected permanent deformations must be estimated as accurately as possible prior to construction in order to secure the serviceability of the structure throughout its service life.

In many cases, the high-cyclic loading leads to multidimensional stress/strain paths in the soil accompanied by phase-shifts between the components. In the case of traffic loads, this is always the case due to the location-variable load sources (Figure 1). As another example, the foundations of offshore wind turbines can
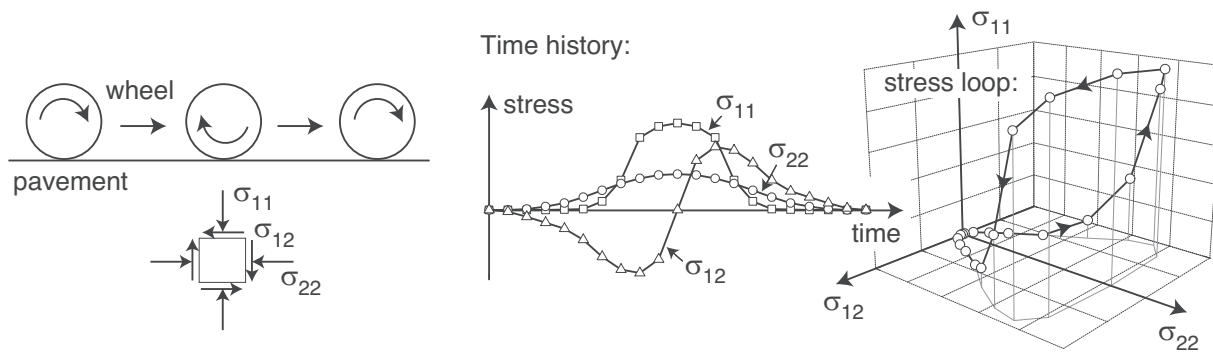
FIGURE 1 | Multidimensional stress acting on a soil element due to locally variable traffic loads [18].
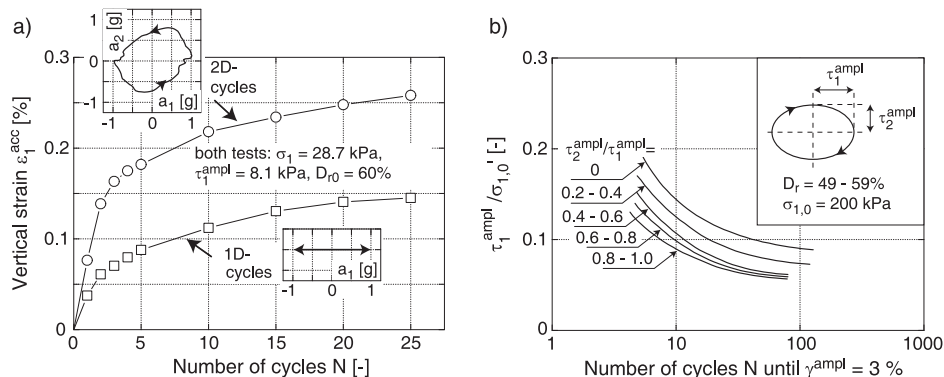

FIGURE 2 | Results from (a) multidimensional vibrating table tests by Pyke et al. [19] on dry sand and (b) multidimensional undrained simple shear tests by Ishihara and Yamazaki [21] on fully water-saturated sand.

be mentioned, where the soil undergoes complex deformation paths around the pile, even if the external loading due to wind and water waves is assumed to be harmonic and in-phase. This is, for instance, highlighted in Ref. [13], where the importance of considering the cyclic rotation of principal stress axes during cyclic loading of a monopile was investigated. Obviously, if a more realistic multidirectional, location-variable, and nonharmonic cyclic loading is to be investigated [14–16], the stress and strain paths become even more complex. The installation of piles may also lead to multidimensional strain paths in the soil, in particular for novel installation techniques with multidirectional pile movement during the driving process as proposed in Ref. [17].

According to several experiments performed on sands, cyclic loading with multidimensional stress or strain loops results in noticeably higher accumulation rates than equivalent (identical *scalar* amplitude) one-dimensional loading [19–27]. This relates to both the buildup of excess pore water pressure under undrained conditions and the accumulation of (volumetric) strain under drained situations. As an example, Figure 2a shows tests on dry sand by Pyke et al. [19] in which two vibrating tables mounted orthogonally on each other were used. Comparing a nearly circular cyclic shear to a uniaxial shear of comparable amplitude, the cumulative vertical strain was about twice as great. The undrained simple shear tests of Ref. [21], the results of which are given in Figure 2b, are another example. Elliptical stress paths were tested, where the amplitude τ_1^{ampl} in the first direction was kept constant, while the amplitude in the second direction was

varied in the range $0 \leq \tau_2^{\text{ampl}} \leq \tau_1^{\text{ampl}}$. With an increasing ratio $\tau_2^{\text{ampl}}/\tau_1^{\text{ampl}}$, that is, with an increasing ovality of the stress loops, a faster accumulation of the excess pore water pressure and thus an earlier attainment of soil liquefaction (described here by the strain criterion $\gamma^{\text{ampl}} = 3\%$) was observed. The majority of the research on sand in the literature referenced above are restricted to just a few cycles ($N \leq 100$) and two-dimensional strain paths. Recent DEM studies are able to reproduce the larger accumulation to multidirectional cyclic loading. According to a DEM study by Yang et al. [28], multidirectional cyclic loading leads to an increased rearrangement of soil particles and greater pore pressure generation in undrained tests. The coordination number and force chains degrade faster under multidirectional loading, leading to an increased accumulation of permanent strain (or excess pore water pressure in undrained tests).

Most element and model tests are performed with uniaxial high-cyclic loading for convenient handling. Furthermore, model approaches for the prediction of long-term deformations due to high-cyclic loading are also designed for one-dimensional loading only. In contrast, the high-cycle accumulation (HCA) model for sand by Niemunis et al. [29] contains a special definition of a multidimensional strain amplitude, which can also be used to capture multidimensional strain paths. The HCA model is an often adopted constitutive model for modeling the soil response to a large number of loading cycles [30, 31], which is particularly used for the analysis of offshore structures such as monopiles

[32–34]. As explained before, complex multidimensional strain paths in the soil around the pile occur during cyclic loading of a pile, for which an adequate multidimensional strain amplitude definition is of great importance.

The definition of the strain amplitude employed in the HCA model was validated by Wichtmann et al. [18] on the basis of triaxial tests with combined axial and lateral cyclic loading as well as simple shear tests for one- and two-dimensional (elliptical and circular) strain paths. A validation for multidimensional loading, both on the element test level and on scale of boundary value problem, is still missing up to now.

The aims of the paper are multifaceted: In the first step, experimental evidence for higher accumulation of permanent strains for stress paths with up to four independent stress components for a number of load cycles much larger then tested in previous work is given. Based on these results, it is demonstrated that the HCA model can account for this effect by its multidimensional strain amplitude definition. Finally, the findings on element test level are transferred to the study of multidirectional loading of piles in small-scale model tests, further validating the HCA model for such load conditions as well as generalizing the HCA model for nonstationary cyclic loading (e.g., frequently changing load amplitudes).

2 | HCA Model

The HCA model for sand by Niemunis et al. [29] is a well-established constitutive model for the simulation of strain accumulation during cyclic loading with a large number of loading cycles (see, e.g., Refs. [31, 33]). Since this work focuses on the strain amplitude definition used in the HCA model, the full set of equations is not presented here. Of relevance for the discussion of the results presented later in this paper is the calculation of the rate of the scalar strain accumulation $\dot{\varepsilon}^{\mathrm{acc}}$, which is given as a product of six functions [29]:

$$\dot{\varepsilon}^{\mathrm{acc}} = f_{\mathrm{ampl}} \, \dot{f}_N \, f_e \, f_p \, f_Y \, f_\pi \qquad (1)$$

According to Equation (1), the rate of strain accumulation is a function of a scalar strain amplitude $\varepsilon^{\mathrm{ampl}}$ (function f_{ampl}), the cyclic preloading ($\dot{f}_N$), the average void ratio e^{av} (f_e), the average mean effective stress p^{av} (f_p), the normalized average stress ratio $\bar{Y}^{\mathrm{av}}$ (f_Y), and the effect of polarization changes (f_π). The term "average" indicates that the quantities are evaluated at the average load (i.e., the trend during the cyclic loading). The equations of the functions can be found in Refs. [29, 35]. Recent experimental findings support the assumption that f_π is of minor importance and can be set to one [35, 36]. The key aspect of this work is the strain amplitude $\varepsilon^{\mathrm{ampl}}$ entering the function f_{ampl} and its influence on the accumulation of permanent strain predicted by the HCA model.

Two-dimensional (2D) stress or strain paths applied in a cyclic DSS or triaxial device lead to larger cumulative strains than 1D paths of same span, according to earlier test series [18, 37]. A particular tensorial formulation of a multidimensional strain amplitude for (up to) 6D convex strain paths is used in the HCA model to take this into account [38]. A process involving
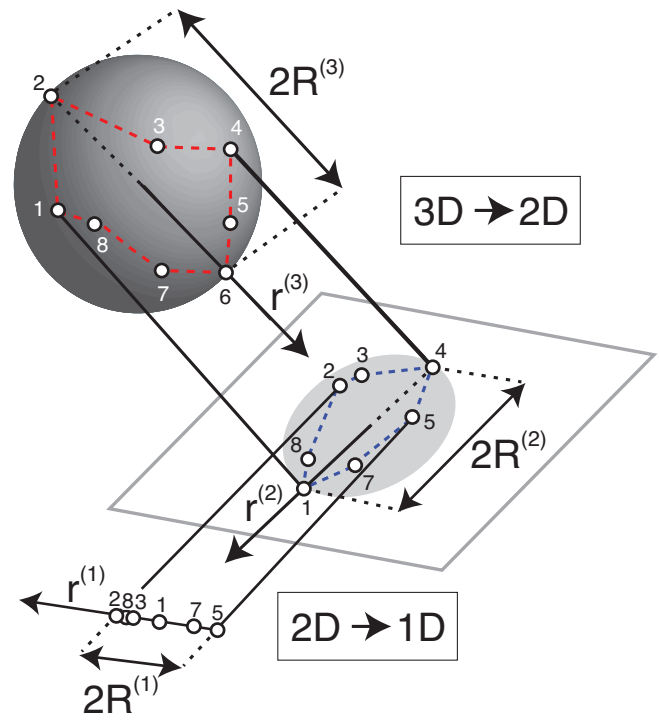

FIGURE 3 | Exemplary projection of a strain loop with eight recorded points from 3D to 2D and from 2D to 1D [38].

numerous projections of the original strain loop yields a scalar value of the strain amplitude $\varepsilon^{\mathrm{ampl}}$. The projections from 3D to 1D are displayed as an illustration in Figure 3. A line connecting the two points of the strain path with the largest distance are identified and the projection is performed in the direction of this line. Finally, $\varepsilon^{\mathrm{ampl}}$ is calculated using the (up to 6) maximum distance values and the accompanying vectors specifying the projection direction. The interested reader is directed to Ref. [38] for more information. So far, only 1D and 2D paths were tested and the amplitude definition of the HCA model validated for Refs. [18, 37]. The experimental program that is the subject of this research was carried out with the intention of extending this validation to up to four-dimensional paths. Four of the six stress or strain tensor components can vary independently in 4D paths. Because even the most advanced technologies in geotechnical laboratories can only test 4D paths, 5D and 6D paths cannot yet be tested.

3 | Experimental Campaign and Accumulation of Strains for Multidimensional Cyclic Loading

3.1 | Experimental Campaign

For all tests presented in the following, "Karlsruhe fine sand" (KFS) has been used as material. KFS is a standard sand used at the geotechnical laboratory of the Karlsruhe Institute of Technology (Germany) (see Ref. [35] for more information), where the tests have been performed.

The experimental campaign comprises three different test device types, three different sample geometries, and two saturation conditions.
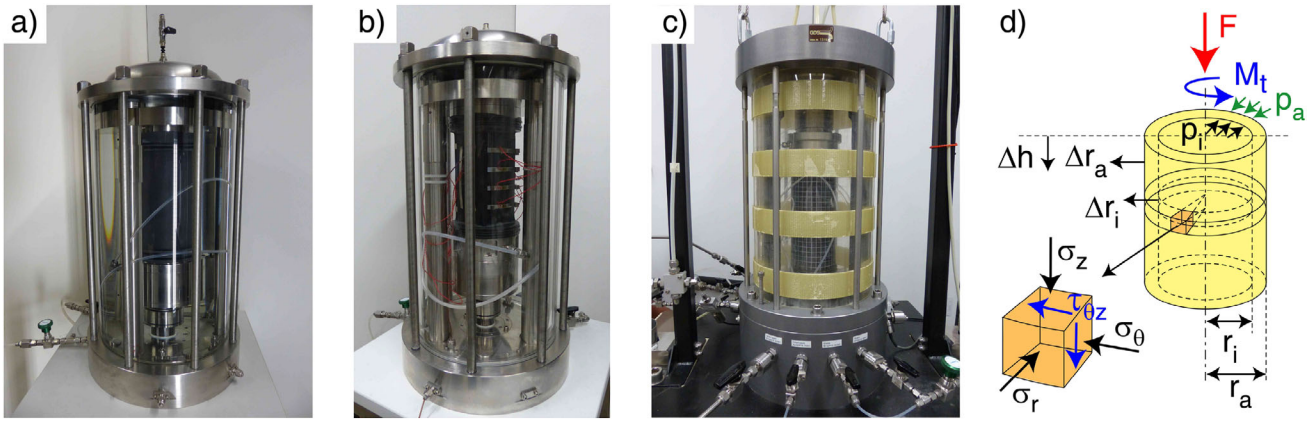
FIGURE 4 | Devices used (a) triaxial device with water-saturated cylindrical samples, (b) triaxial device with local strain measurements using LDTs on dry cuboid-shaped samples, (c) hollow cylinder device, and (d) external loads and stresses acting on an element of soil in the hollow cylinder test (reprinted from Ref. [36]).

Sixty-four tests were conducted in a cyclic triaxial device. The triaxial devices (Figure 4a,b) allow for the simultaneous cyclic variation of effective axial stress (via the load piston) and effective lateral stress (by cyclic variation of cell or pore pressure). This permits the application of 1D stress paths with different inclinations in the P–Q plane as well as 2D stress paths. The cyclic alteration of cell pressure is required for the application of 2D stress paths, which may result in membrane penetration effects [39–41]. By using local strain measurements, it is possible to eliminate these and other sources of flaws in global deformation measurements (such as system compliance and bedding error). Therefore, 26 additional tests on air-pluviated samples have been carried out for comparison purposes in a cyclic triaxial apparatus but with local measurements of deformation on cuboid-shaped samples ($a \times b = 90 \times 90$ mm^2, $h = 180$ mm). LDTs (local deformation transducers), that is, soft leaf spring–like strips of stainless steel equipped with strain gauges (Figure 4b) were applied for that purpose. The details of the used LDTs along with the calibration procedure are presented in Refs. [36, 42, 43]. Details on the testing program including the visualization of the applied 1D or 2D stress paths in Figure A.1 can be found in Appendix A. Appendix B summarizes the results of the comparison of the air-pluviated samples with local strain measurements (26 tests) and the tests with fully water-saturated full cylinder samples with global strain measurements (64 tests). From these results in can be concluded that the strain amplitudes obtained from the local strain measurements on dry cuboid-shaped samples are slightly smaller than those derived from the global deformation records in case of fully water-saturated cylindrical samples.

Thirty additional tests were performed in a GDS hollow cylinder triaxial device (Figure 4c). The samples had an outer diameter $d_a = 100$ mm, an inner diameter $d_i = 60$ mm, and a height $h = 200$ mm. The volume changes of the hollow cylinder samples were measured via the pore water. Thus, the samples were tested fully water-saturated.

The hollow cylinder device allows to study paths with up to four independent stress paths [44]. For this, the vertical force F, torsional moment M_T, outer cell pressure p_a, and inner cell pressure p_i (Figure 4d) can be controlled, allowing for oscillations of three normal stresses (σ_z in vertical, σ_r in radial, and σ_θ in

circumferential direction) and one shear stress component $\tau_{\theta z}$. By rotating the coordinate system by the angle α, these four stresses can be expressed by three major stresses: σ_1, σ_2, and σ_3.

In the cyclic triaxial tests on water-saturated cylindrical and dry cuboid-shaped samples, 1D, 2D elliptical, and 2D circular stress paths were applied in the P–Q plane, while 2D to 4D paths were tested using the hollow cylinder device. The applied stress paths in the hollow cylinder device are exemplified in Figure A.2 of Appendix A. All stress paths maintained a sufficient distance from the failure lines. In all tests, cycles were applied at an average mean effective stress of $p^{\mathrm{av}} = 200$ kPa and an average mean stress ratio of $\eta^{\mathrm{av}} = 0.50$. Samples were prepared with initial relative densities of $D_{r0} \approx 40\%$ and 70%. For water-saturated samples, a back pressure of 500 kPa was used. The first, or "irregular," cycle, typically causing larger deformations, was applied at a lower frequency (0.01 Hz). The subsequent 10^4 regular cycles were applied at 0.02 Hz. Since the HCA model predicts strain accumulation rates only for the regular cycles, the first irregular cycle is excluded from this paper. Here, $N = 1$ refers to the end of the first regular cycle.

3.2 | Results and Discussion

The tests are evaluated in terms of the isometric variables $P = \sqrt{3}p$, $Q = \sqrt{3/2}q$, $\varepsilon_P = \varepsilon_v/\sqrt{3}$, and $\varepsilon_Q = \sqrt{3/2}\varepsilon_q$. Note that some of the results have already been presented in Ref. [45].

The left-hand side of Figure 5 exemplary shows the results of the three different devices for the same circular stress path. From Figure 5b, it is clear that the resulting strain path is not perfectly identical for the different devices. However, this is not only because of the different devices but also due to the sample preparation process and saturation conditions (dry in case of the cuboid sample). These differences are further highlighted in Figure 5c where the strain amplitudes calculated using the procedure described in Section 2 are plotted. The smallest strain amplitude is observed for the dry cuboid-shaped samples, whereas the hollow cylinder test shows the largest strain amplitude. Larger strain amplitudes lead to larger rates of strain accumulation as can be seen from Figure 5d, at least for $N > 100$.
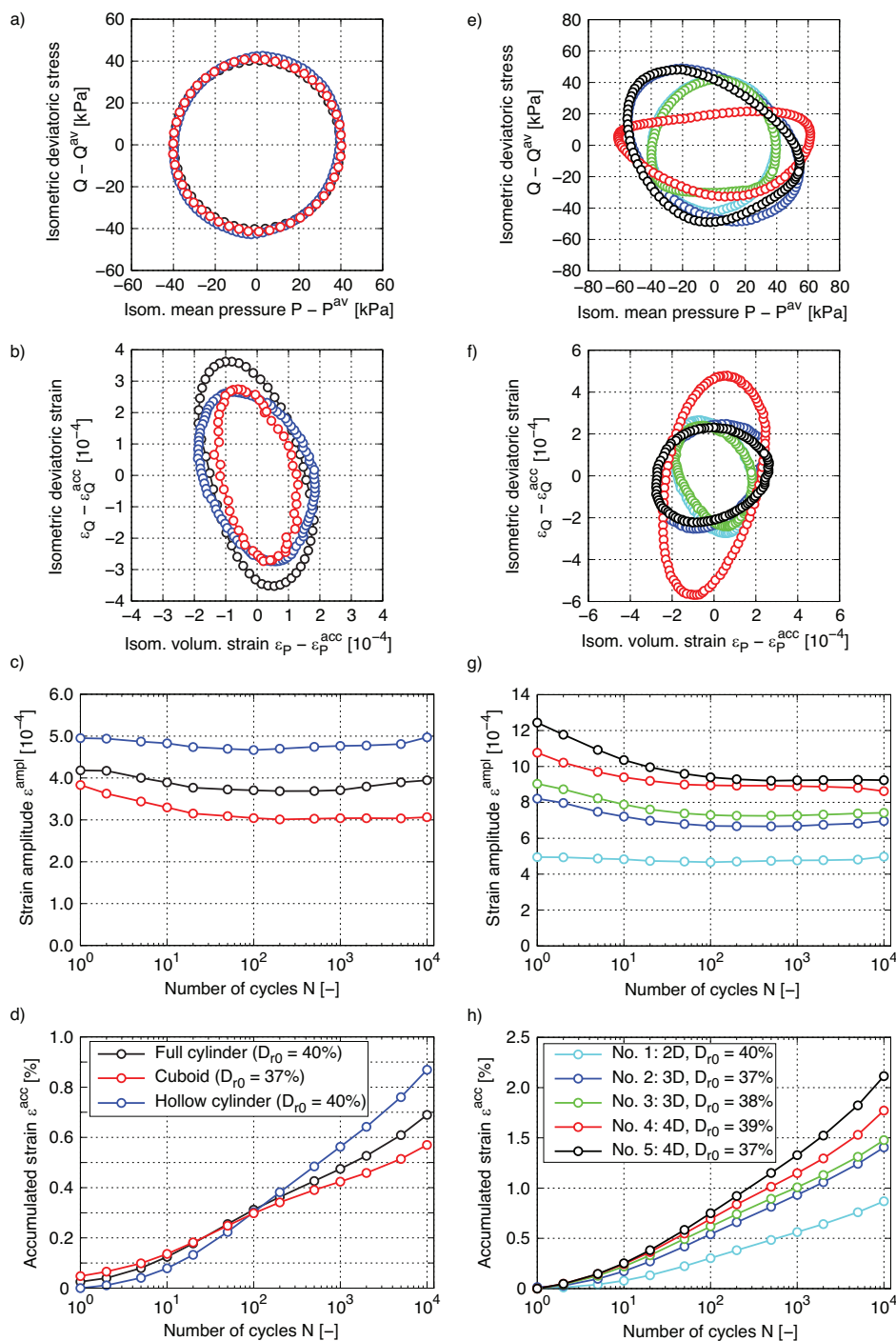
FIGURE 5 | Left column: Results of the different test set-ups for the same circular cyclic stress path given in plot a). Right column: Results obtained from the hollow cylinder device applying the stress paths listed in Table 1: a,e) Prescribed P-Q stress paths, b,f) Resulting ε_P-ε_Q strain paths during one cycle at $N = 10,000$, c,g) Measured strain amplitude ε^{ampl} during the tests and d,h) Accumulated permanent strain ε^{acc} with increasing number of cycles N in tests on medium dense samples ($D_{r0} \approx 40\%$).

The right column of Figure 5 shows the influence of 2D, 3D, or 4D stress paths on the strain amplitude and the accumulation of strains in tests using the hollow cylinder device only. Five different tests are considered, for which the applied stresses and the phase shifts of the sinusoidal signal of the oscillating stress components are given in Table 1. All remaining variables such as initial density or sample preparation technique were the same for all tests.

As can be seen from Figure 5, the smallest values of ε^{ampl} and of ε^{acc} were obtained for the 2D stress path, while the largest values resulted from the 4D one. Thus, with increasing dimensionality of the stress path, both the strain amplitudes ε^{ampl} and the accumulated strains ε^{acc} grow.

All of the 120 performed tests had the same average mean effective stress $p^{av} = 200$ kPa and average mean stress ratio $\eta^{av} = 0.5$.

TABLE 1 | Program of the cyclic hollow cylinder tests with 2D, 3D, and 4D stress paths.

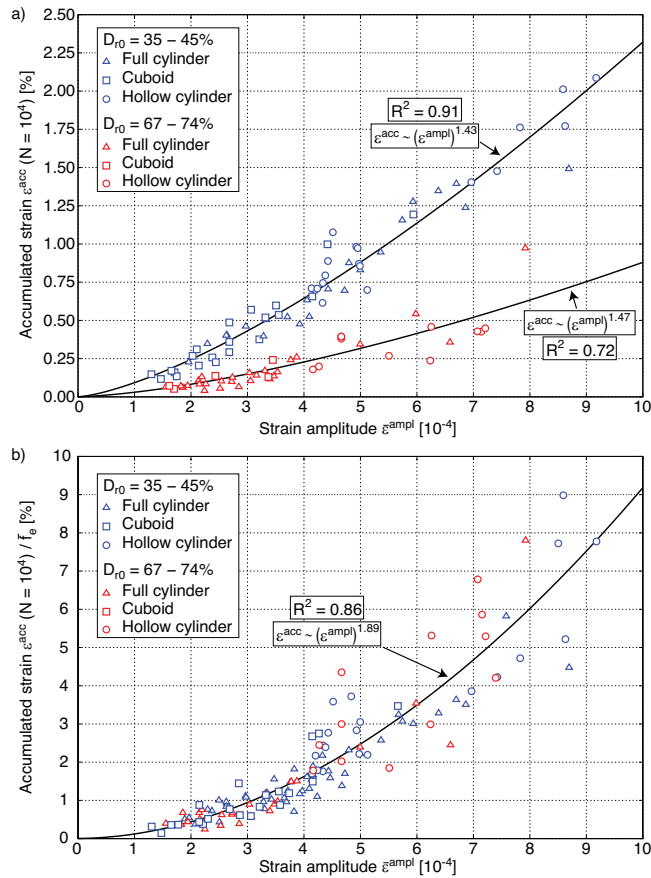| No.	Dimension	Stress amplitudes				Phase shifts			
		σ_z^{ampl} [kPa]	σ_r^{ampl} [kPa]	σ_θ^{ampl} [kPa]	$\tau_{\theta z}^{ampl}$ [kPa]	ϕ_{σ_z} [°]	ϕ_{σ_r} [°]	ϕ_{σ_θ} [°]	$\phi_{\tau_{\theta z}}$ [°]
1	2D	40.00	28.28	28.28	0.00	35.26	125.26	125.26	0.00
2	3D	40.00	28.28	56.56	0.00	35.26	125.26	125.26	0.00
3	3D	40.00	28.28	28.28	28.28	35.26	125.26	125.26	0.00
4	4D	40.00	28.28	56.56	28.28	35.26	125.26	62.63	62.63
5	4D	40.00	28.28	56.56	28.28	35.26	125.26	125.26	125.26

FIGURE 6 | (a) Accumulated strain ε^{acc} after 10,000 cycles versus average strain amplitude $\bar{\varepsilon}^{ampl}$ for each of the 120 tests considering the three different test devices and two different initial relative densities D_{r0}. (b) Same as plot (a) but with normalization of the accumulated strain by the function $\bar{f}_e$ of the HCA model to detach the influence of relative density from the tests.

Therefore, according to the HCA model and its definition of the strain amplitude, the accumulated strain for each of the tests can be solely expressed in terms of its strain amplitude and density. The validity of this is demonstrated in Figure 6a, where the accumulated permanent strains ε^{acc} after 10,000 cycles from all 120 tests are given as a function of the strain amplitude $\bar{\varepsilon}^{ampl}$ of that test. The strain amplitudes have again been calculated using the procedure described in Section 2. Because the strain amplitude slightly changes during the cyclic

loading (see Figure 5c,g), a mean value over 10,000 cycles is used. Since the tests have been performed with two different values of initial density, the diagram contains data for $D_{r0} \approx 40\%$ and $D_{r0} \approx 70\%$. For a certain density, the ε^{acc}–$\bar{\varepsilon}^{ampl}$ data for the different types of samples, saturation conditions, and dimensionality of the stress or strain path (1D up to 4D) can be approximated by one function. Thus, the definition of the strain amplitude according to Ref. [38] allows the description of the ε^{acc}–$\bar{\varepsilon}^{ampl}$ relationship by a single function, which can be validated with the coefficient of determination R^2 as the deviation of the points from the curve. The amplitude function of the HCA model $\varepsilon^{acc} \sim (\bar{\varepsilon}^{ampl})^n$ has been fitted to the data, leading to exponents $n = 1.43$ with $R^2 = 0.91$ for $D_{r0} = 40\%$ and $n = 1.47$ with $R^2 = 0.72$ for $D_{r0} = 70\%$. The influence of the different relative densities on the accumulated strain ε^{acc} can be eliminated by division with the void ratio function of the HCA model $\bar{f}_e$ (which is the average value of the function f_e of the different tests, for the definition of f_e, see, e.g., Ref. [29]), evaluated with an average value of the void ratio $\bar{e}$ over 10,000 cycles. The resulting plot of ε^{acc} versus $\bar{\varepsilon}^{ampl}$ is given in Figure 6b. The data in Figure 6b can again be described by $\varepsilon^{acc}/\bar{f}_e \sim (\bar{\varepsilon}^{ampl})^n$, resulting in an exponent $n = 1.89$ and a coefficient of determination $R^2 = 0.86$.

Therefore, it can be concluded that the amplitude definition used in the HCA model can appropriately consider the effect of multidimensional strain paths from 1D to 4D conditions on the accumulated strain.

4 | Long-Term Cyclic Response of Piles Subjected to Multidirectional Loading

The relevance of the multidimensional definition of the strain amplitude employed in the HCA model for practical applications is demonstrated in this section by means of the analysis of the long-term cyclic response of monopile foundations subjected to multidirectional loading. From small-scale lab tests and centrifuge modeling, it has been generally found that multidirectional cyclic loading causes higher accumulation of deformation for pile foundations compared to an equivalent unidirectional cyclic loading [15, 46, 47]. As has been demonstrated in the previous section, this effect can be captured by the HCA model, at least at the element test level.

In order to verify if the HCA model can also adequately reproduce effects resulting from multidirectional cyclic loading of pile
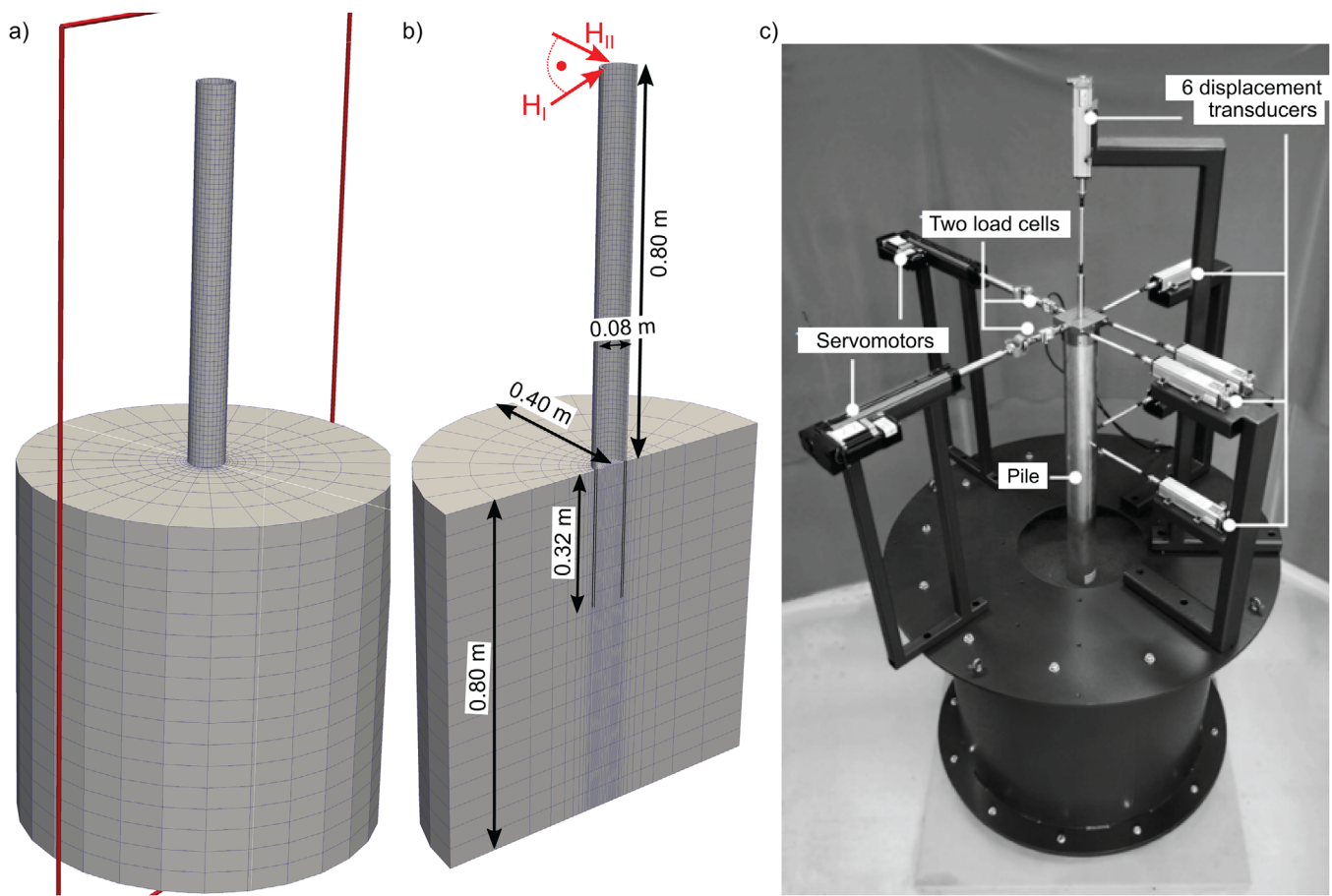
FIGURE 7 | (a) and (b) Dimensions, finite-element mesh, and loading by H_I, H_{II} of the model tests. (c) Photo of the device (reprinted from Ref. [15]).

foundations for offshore wind farms, the back-analysis of 1-g small-scale model tests with multidirectional loading performed by Richards et al. [15] is discussed in the following.

4.1 | Model Tests by Richards et al.

Foundations of offshore structures are subjected to lateral cyclic loading with a continual variation of wind and wave directions, which has been investigated in model tests on single piles by Richards et al. [15]. The tests have been performed at the facilities of Oxford University, building upon the earlier tests performed by Leblanc et al. [48]. The dimensions of the small-scale model test are displayed in Figure 7a,b and the experimental setup is depicted in Figure 7c. The pile dimensions were scaled at a ratio of 1:100. A pile made of aluminum has been used to adjust for the reduced pile rigidity in the model scale. The pile had a length of $L = 320$ mm embedded in the sand, an outer diameter of $D = 80$ mm, and a wall thickness of $t = 5$ mm.

With an average surface roughness of $R_a = 0.6$ μm, the pile's surface was deemed to be smooth. After the sand had been poured into a cylinder with an 800-mm diameter and an 800-mm height, the pile was installed to the desired embedment depth using drop weights, mimicking the process of impact driving. At a height of $h = 800$ mm above the top surface of the sand, lateral loading in two orthogonal directions (forces H_I, H_{II}) was applied. For the

tests taken into account in the back-analysis, dry Yellow Leighton Buzzard sand with an initial relative density of $D_{r0} = 60\%$ before the installation of the pile was used.

4.2 | Back-Analysis

The back-analysis of the tests includes two major processes: pile installation and subsequent multidirectional lateral cyclic loading. Previous investigations by the authors [49–51] and other researchers [52, 53] found a distinct influence of the pile installation effects on the response to subsequent (cyclic) loading, in particular for unsaturated or dry sandy soils. Because during cyclic lateral loading, the mobilized soil zone around the pile is much smaller than for monotonic loading to ultimate capacity, a larger influence of the installation process on the cyclic response compared to the monotonic capacity is expected [54]. Therefore, the pile installation performed in the model tests by Richards et al. is simulated prior to the cyclic lateral loading. The hypoplastic model with intergranular strain extension [55, 56] is adopted as constitutive model to simulate the installation process.

For the required calibration of material parameters of the hypoplastic model with intergranular strain extension and the HCA model, the Yellow Leighton Buzzard sand was tested in an extensive laboratory testing program (also at Karlsruhe Institute

of Technology). A large number of oedometric compression, drained monotonic triaxial, undrained cyclic triaxial and drained triaxial tests with high-cyclic loading (100,000 cycles) were performed. Most of the tests were performed and evaluated in the range of low effective stress to best represent the low stress level prevailing in the 1-g model tests. Staubach et al. [50] reports the full calibration of the parameters for the hypoplastic model with intergranular strain extension and of the HCA model for the yellow Leighton-Buzzard sand. Although parameter calibration has been performed using triaxial tests conducted at low stress levels (as low as 20 kPa initial mean effective stress), a systematic investigation into the uncertainties introduced by these low stress levels in numerical analyses is still lacking. While Richards et al. [57] examined the effect of stress level on the accumulation of deformations, they did not address the impact of installation effects. One of the key findings from the study is that as stress levels increase, the rate of displacement accumulation and the rate of change in secant stiffness under cyclic loading decrease. These stress-dependent effects imply that tests conducted at low stress levels, such as 1-g tests, may overestimate displacement and underestimate monopile stiffness, leading to uncertainties when extrapolating results to full-scale applications, though not necessarily in the numerical modeling of such tests. Further research in this area is certainly needed.

4.3 | Pile Installation

The simulation of the pile installation process is only briefly discussed in the following, since the focus of the paper is on multidirectional cyclic loading. For more information and detailed discussion on the adopted numerical schemes, the interested reader is referred to the simulation of the model tests by Leblanc et al. [48] reported by the authors in Ref. [50], where a similar test set-up as in the tests by Richards et al. has been used.

The coupled Eulerian–Lagrangian (CEL) approach, implemented in the finite-element program Abaqus, is used to simulate the installation of the pile. The contact between a Lagrangian body and Eulerian elements can be taken into account using the CEL approach. The soil is represented using Eulerian elements, allowing to model very large deformations, because it deforms significantly during the installation of the piles. Lagrangian elements are used to represent the pile that penetrates the soil.

In the numerical analysis, the pile was jacked rather than impact-driven. This is because it is not possible to consider several hundreds of blows in the numerical model since the process is modeled in physical time and time integration is performed with small time increments in explicit fashion (the time increment is approximately 10^{-5} s for the simulations performed in this work). For the model tests of Leblanc et al. [48], Staubach et al. [50] investigated the influence of jacking versus impact driving. Following installation, the responses of the piles to lateral loads were comparable for the two installation methods. Therefore, it seems acceptable to assume that jacking causes similar changes in the soil's state as impact driving for the present analyses. However, this should not be regarded as a general rule and depends on a number of factors such as the specifications of the pile drivers. A jacking velocity of 0.06 m/s is adopted in the analyses presented here.

Figure 8 depicts the evolution of the mean effective stress and relative density for two penetration depths, $t = 10$ cm and $t = 25$ cm. During installation, there is a reduction in relative density at and a heaving of the ground surface. The majority of the compacted area is located inside the pile, with strong compaction concentrated around the pile tip.

Under the pile tip, the mean effective stress rises noticeably. For $t = 10$ cm, the largest values are seen immediately beneath the pile tip. The pile penetration results in an increase of almost factor 100 compared to the pre-installation mean stress at this depth. The distribution at a penetration depth of $t = 25$ cm shows that as pile penetration continues, the volume of soil below the pile tip with mean effective stresses greater than 100 kPa grows. High stresses are seen very near the model's symmetry axis, almost touching the bottom model boundary, indicating that there are some effects from the container boundaries. However, this being also the case in the model tests, no impact on the outcomes of the comparisons between experiments and simulations presented in the next section is expected.

It can be concluded that the installation process changes the soil state considerably. A comparison of the lateral loading behavior with and without the consideration of the installation process can be found in Refs. [50, 58]. Neglecting the installation process generally led to too large pile rotations in the simulations compared to the experiments. Given the objectives of the present work, only simulations of the lateral loading of the pile considering the installation process are performed.

4.4 | Multidirectional Cyclic Lateral Loading

Lagrangian elements for both pile and soil as well as an implicit time integration are used to simulate the pile's lateral loading. The finite element program `numgeo` is utilized (see www.numgeo.de [54, 59–61]). The state variables after installation are imported in the full cylindrical model depicted in Figure 7a following the procedures described, for example, in Refs. [50, 62].

Only the model tests with so-called *fan-type loading* are considered in the back-analysis. For reference, one test with equivalent unidirectional loading is analyzed in addition. For the fan-type loading, the moments M_I, M_{II} at ground surface resulting from the two horizontal forces H_I, H_{II} depicted in Figure 7b are both varying with number of load cycles. Moreover, not only the amplitudes of the moments vary, but also their average values. The ratio of the two moments is quantified by the *spread angle* Φ, which denotes the angle between the two moments at their respective maximum. For unidirectional cyclic loading, $\Phi = 0°$ holds. Figure 9 depicts the time history of the two moments for fan-type loading with $\Phi = 30°$ and $\Phi = 90°$, respectively. The moments are calculated according to Ref. [15] by

$$M_I = \frac{M_R}{10}[1 + \sin(2\pi t)] \cdot \cos\left[\Phi \sin\left(\frac{2\pi t}{100}\right)\right] \quad (2)$$

$$M_{II} = \frac{M_R}{10}[1 + \sin(2\pi t)] \cdot \sin\left[\Phi \sin\left(\frac{2\pi t}{100}\right)\right], \quad (3)$$

where M_R is the moment required for a static rotation of the pile of $\Theta_R = 2°$, that is, the ultimate pile resistance. M_R is set identical
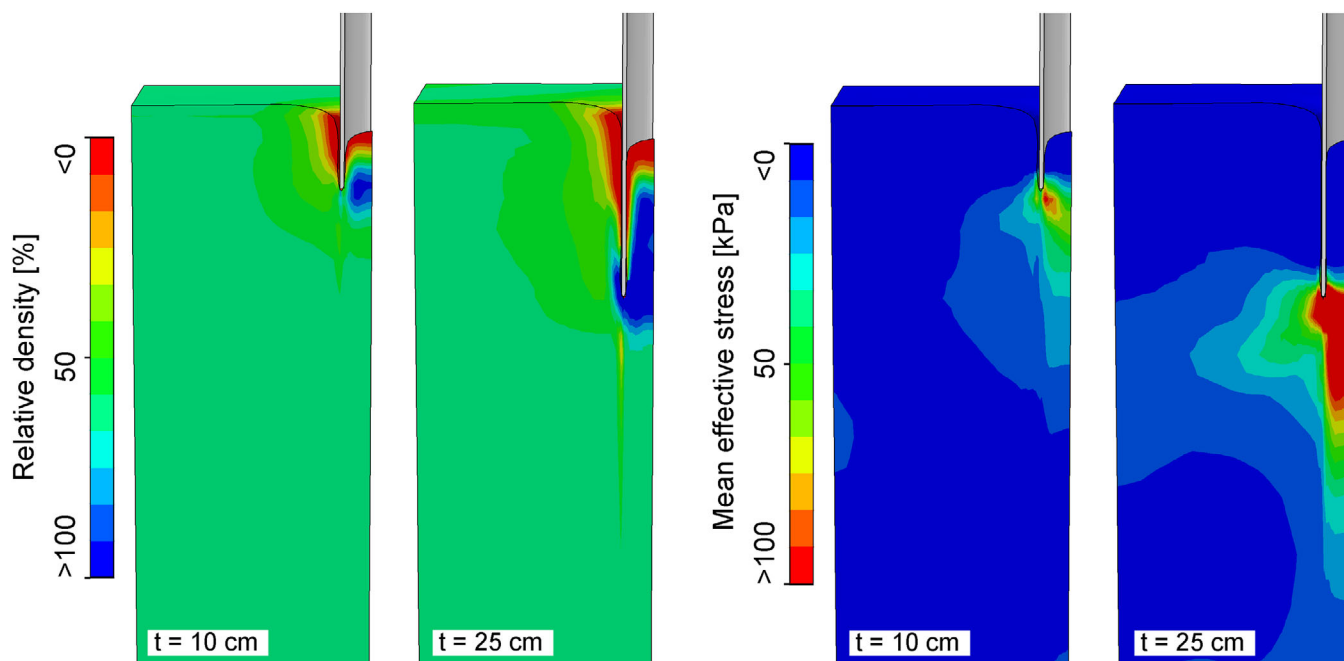
FIGURE 8 | Spatial distributions of relative density and mean effective stress after a penetration of the pile of $t = 10$ cm and $t = 25$ cm, respectively.
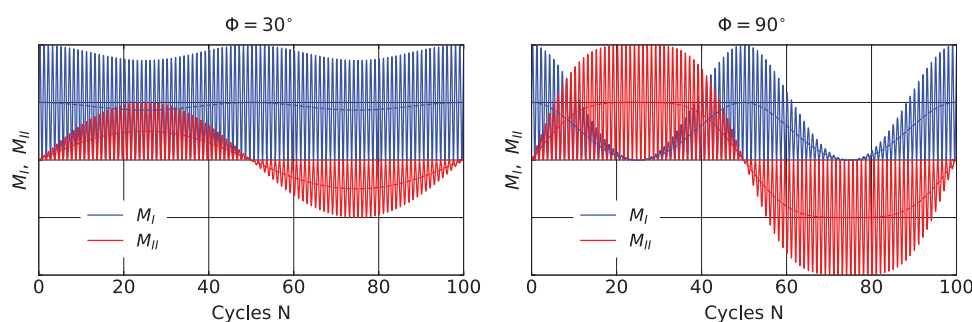

FIGURE 9 | Fan-type loading for spread angles $\Phi = 30°$ and $\Phi = 90°$, respectively.

to the one measured and reported in Ref. [15]. According to Equations (2) and (3), a sinusoidal change of the loading direction with a frequency of 0.01 Hz is considered, which overlies the individual cyclic loading, which has a frequency of 1 Hz. Note that there are no rate effects being considered in the analyses, that is, static analyses are performed.

The fan-type loading is not straight-forward to be modeled with the HCA model because the cyclic loading does not remain constant during one "sweep" (100 cycles). Only if the loading direction would change with the same frequency as the frequency of the cyclic loading, a direct application of the HCA model is possible. Therefore, it is not directly clear how to define the strain amplitude required for the HCA model. In fact, this is an often mentioned drawback of "high-cycle" strategies such as followed by the HCA model.

To resolve this issue, it is proposed to use multiple strain amplitudes to account for the change in the amplitudes during the change of loading direction. Since one "sweep" consists of 100 cycles, 100 different strain amplitudes are considered in the HCA analyses. For this purpose, one "sweep" is simulated

using the hypoplastic model with intergranular strain extension [55, 56] and for each cycle, the strain path is recorded. One hundred strain amplitudes are then calculated according to the procedures described in Section 2. Because the hypoplastic model with intergranular strain extension is not suitable to calculate the accumulation of strains for a larger number of load cycles, the simulation with the HCA model is not performed subsequently to the determination of the strain amplitudes but in a second model. The initial state in the second model corresponds to the one following the pile installation process and uses the 100 strain amplitudes calculated in the first model as input. Therefore, the changed state variables (stress and void ratio) due to 100 cycles calculated with the hypoplastic model with intergranular strain extension are not considered in the simulation with the HCA model and all cycles are simulated with the HCA model. In a conventional HCA simulation with a single strain amplitude, this approach would be feasible as well, but the impact would be minor due to the low accumulation of strain from just one cycle simulated using the hypoplastic model with intergranular strain extension. This is not the case when simulating 100 cycles, where the influence becomes significant necessitating the approach adopted here.
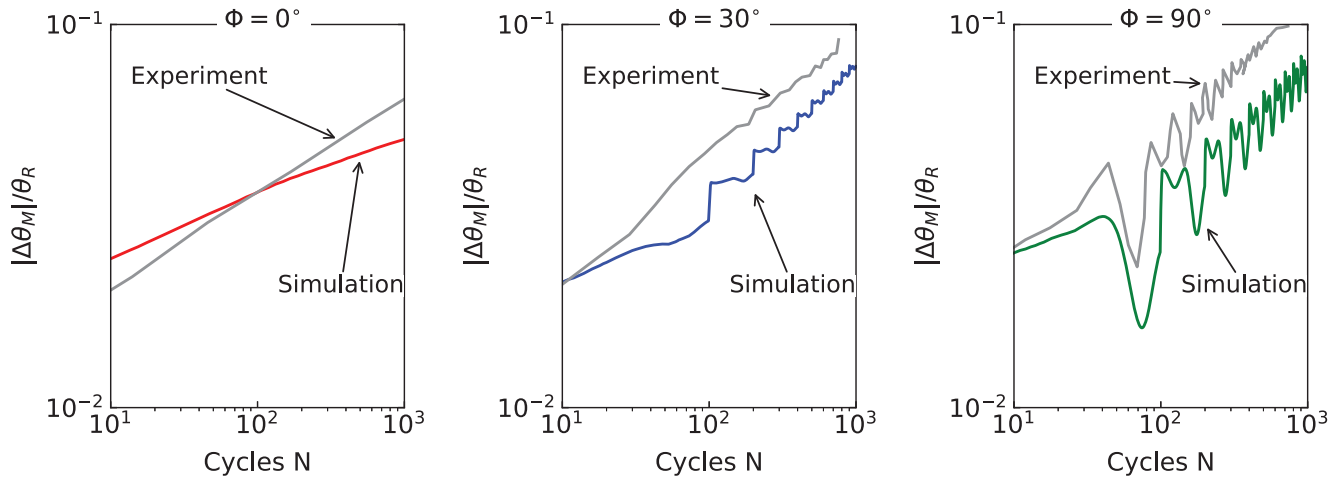
FIGURE 10 | Magnitude of change of rotation during cyclic loading divide by the reference rotation at ultimate capacity ($\Theta_R = 2°$) for different *spread angles* Φ for the simulations and the results of the corresponding experiments reported by Richards et al. [15].

In the HCA calculation, the strain amplitude changes with number of loading cycles with a frequency according to the model tests. At the same time, the average values of the moments change during the HCA phase according to Equations (2) and (3). Because both the strain amplitudes and the average values of the moments change during the HCA-phase, the time increment can not be chosen arbitrarily. A fixed time increment of $\Delta N = 1$ is used in the HCA calculation. No interpolation of the 100 strain amplitudes is required and for each of the cycles, the "correct" strain amplitude is used. Note that this is still computationally superior to modeling the cyclic loading cycle-by-cycle with multiple increments per cycle (without defining a strain amplitude, see, e.g., Ref. [63]) since only one increment per cycle has to be calculated. In accordance with the model tests, 10 "sweeps" are simulated with the HCA model according to the procedure described, resulting in a total of 1000 cycles analyzed.

Figure 10 shows the change of mean rotation during the cyclic loading normalized by the reference rotation at ultimate capacity ($\Theta_R = 2°$) for the experiments and corresponding simulations for different values of the spread angle Φ. As noted by Richards et al. [15], the change of the loading angle leads to "ripples" in the curves of the experiment. These "ripples" are also seen for the simulations since the loading direction does change during the high-cycle phase. Therefore, the results of the experiments and the simulations are directly comparable in Figure 10 since both show the trend of rotation during the cyclic loading.

For unidirectional loading ($\Phi = 0$), a slightly too low accumulation can be seen in Figure 10, while the rotation due to the first cycles is too high compared to the experiment. Higher accumulation rates are observed for the fan-type loading, for both the experiments and the simulations. With increasing value of Φ, larger accumulation of rotation occurs for almost all number of load cycles. In line with the simulation of the unidirectional loading, the accumulation rates are slightly too low for the simulations with $\Phi \neq 0$. This could be due to the parameters of the HCA model, some of which were only estimated on the basis of correlations [50]. However, the important aspect, higher rates of accumulation for $\Phi \neq 0$, is generally captured well by

the simulations. The large "ripple" in the test with $\Phi = 90°$ at $N = 80$ can be reproduced in the simulation as well. Therefore, it can be concluded that the HCA model allows to consider the effect of multidimensional loading on the accumulated rotation adequately. In addition, the proposed scheme of considering multiple strain amplitudes can appropriately capture a nonstationary cyclic load in the simulation.

5 | Conclusions

In this work, the current state of knowledge on multidimensional cyclic loading of soils was extended by element tests with up to four-dimensional drained cyclic loading and 10,000 cycles in a hollow cylinder triaxial device. It is demonstrated that with increasing dimensionality, an increase of accumulation of permanent strain occurs. This can be accounted for in the HCA model by means of its multidimensional strain amplitude definition, which was validated by the experimental data. A unique relation between accumulated strain and multidimensional strain amplitude was found independent of the dimensionality of the stress or strain loop, of the sample geometry and the saturation state and can be described by the relation $\varepsilon^{acc} \sim (\varepsilon^{ampl})^n$. In this respect, based on the test results, the definition of the multidimensional strain amplitude can be regarded as validated for one- to four-dimensional strain paths. By the back-analysis of small-scale model tests on piles subjected to multidirectional lateral loading, it was further demonstrated that the HCA model can also adequately reproduce the effects of multidirectional loading in a complex boundary value problem. It could be shown that location-variable cyclic loading can be modeled with the HCA model when multiple strain amplitudes are accounted for. In line with the results of the model tests, permanent pile rotations increased with increasing dimensionality of the cyclic loading.

Disclosure

The tests have been performed by the technician H. Borowski in the soil mechanics laboratory at the institute in Karlsruhe.

Data Availability Statement

The data that support the findings of this study are available from the corresponding author upon reasonable request.

References

1. S. Yin, P. Liu, L. Kong, X. Zhang, Y. Qi, and J. Huang, "Accumulated Plastic Strain Behavior of Granite Residual Soil Under Traffic Loading," *Soil Dynamics and Earthquake Engineering* 164 (2023): 107617, https://doi.org/10.1016/j.soildyn.2022.107617.

2. C. Pasten, H. Shin, and J. Santamarina, "Long-Term Foundation Response to Repetitive Loading," *Journal of Geotechnical and Geoenvironmental Engineering, ASCE* 140, no. 4 (2014): 04013036.

3. P. Staubach, D. Wegener, J. Machaček, and T. Wichtmann, "Long-Term Settlement of Dynamically Loaded Shallow Foundations," *International Journal of Geomechanics, ASCE* 24, no. 6 (2023): 04024099, https://doi.org/10.1061/IJGNAI.GMENG-8977

4. C. Abadie, B. Byrne, and G. Houlsby, "Rigid Pile Response to Cyclic Lateral Loading: Laboratory Tests," *Géotechnique* 69, no. 10 (2019): 863–876.

5. J. Machaček, T. Wichtmann, H. Zachert, and T. Triantafyllidis, "Long-Term Settlements of a Ship Lock: Measurements vs. FE-Prediction Using a High Cycle Accumulation Model," *Computers and Geotechnics* 97, no. 5 (2018): 222–232.

6. V. Osinov, S. Chrisopoulos, and C. Grandas Tavera, "Vibration-Induced Stress Changes in Saturated Soil: A High-Cycle Problem," in *Holistic Simulation of Geotechnical Installation Processes - Benchmarks and Simulations*, Lecture Notes in Applied and Computational Mechanics, vol. 80, ed. T. Triantafyllidis (Cham, Switzerland: Springer, 2015), 69–84.

7. P. Staubach, I. Kimmig, J. Machaček, T. Wichtmann, and T. Triantafyllidis, "Deep Vibratory Compaction Simulated Using a High-Cycle Accumulation Model," *Soil Dynamics and Earthquake Engineering* 166, no. 3 (2023): 107763, https://doi.org/10.1016/j.soildyn.2023.107763.

8. K. Mallwitz and U. Holzlöhner, "Verfahren zur Ermittlung der Setzung von Fundamenten infolge zyklischer Beanspruchung," *Bautechnik* 73, no. 3 (1996): 175–186.

9. H.-J. Heller, "Bauwerkssetzungen bei sandigem Untergrund infolge von Erschütterungen durch Bahnverkehr," *Baumaschine und Bautechnik* 35, no. 2 (1981): 56–61.

10. H.-J. Heller, "Setzungen von Kranbahnstützen infolge von Lastwechseln bei sandigem Untergrund," *Bautechnik* 72 (1995): 11–19.

11. P.-A. von Wolffersdorff and R. Schwab, "Schleuse Uelzen I - Hypoplastische Finite-Elemente-Analyse von zyklischen Vorgängen," *Bautechnik* 78, no. 11 (2001): 771–782.

12. J. Chai and N. Miura, "Traffic-Load-Induced Permanent Deformation of Road on Soft Subsoil," *Journal of Geotechnical and Geoenvironmental Engineering, ASCE* 128, no. 11 (2002): 907–916.

13. X. Cheng, A. Diambra, E. Ibraim, H. Liu, and F. Pisano, "3D FE-Informed Laboratory Soil Testing for the Design of Offshore Wind Turbine Monopiles," *Journal of Marine Science and Engineering* 9 (Jan 2021): 101, https://doi.org/10.3390/jmse9010101.

14. A. M. Page, G. Grimstad, G. R. Eiksund, and H. P. Jostad, "A Macro-Element Model for Multidirectional Cyclic Lateral Loading of Monopiles in Clay," *Computers and Geotechnics* 106 (2019): 314–326, https://doi.org/10.1016/j.compgeo.2018.11.007.

15. I. A. Richards, B. W. Byrne, and G. T. Houlsby, "Monopile Rotation Under Complex Cyclic Lateral Loading in Sand," *Geotechnique* 70, no. 10 (2020): 916–930, https://doi.org/10.1680/jgeot.18.P.302.

16. C. N. Abadie, W. J. A. P. Beuckelaers, B. W. Byrne, G. T. Houlsby, H. J. Burd, and R. McAdam, "Modeling Lifetime Performance of Monopile Foundations for Offshore Wind Applications," *Journal of Geotechnical and Geoenvironmental Engineering* 149, no. 8 (2023): 04023051, https://doi.org/10.1061/JGGEFK.GTENG-9833.

17. E. Kementzetzidis, F. Pisano, A. Tsetas, and A. V. Metrikine, "Gentle Driving of Piles at a Sandy Site Combining Axial and Torsional Vibrations: Quantifying the Influence of Pile Installation Method on Lateral Behavior," *Journal of Geotechnical and Geoenvironmental Engineering* 149, no. 11 (2023): 04023102, https://doi.org/10.1061/JGGEFK.GTENG-11179.

18. T. Wichtmann, A. Niemunis, and T. Triantafyllidis, "On the Influence of the Polarization and the Shape of the Strain Loop on Strain Accumulation in Sand Under High-Cyclic Loading," *Soil Dynamics and Earthquake Engineering* 27, no. 1 (2007): 14–28.

19. R. Pyke, H. Seed, and C. Chan, "Settlement of Sands Under Multidirectional Shaking," *Journal of the Geotechnical Engineering Division, ASCE* 101, no. GT4 (1975): 379–398.

20. H. Seed, R. Pyke, and G. Martin, "Effect of Multidirectional Shaking on Pore Pressure Development in Sands," *Journal of the Geotechnical Engineering Division, ASCE* 104, no. GT4 (1978): 27–44.

21. K. Ishihara and F. Yamazaki, "Cyclic Simple Shear Tests on Saturated Sand in Multi-Directional Loading," *Soils and Foundations* 20, no. 1 (1980): 45–59.

22. Y. Yamada and K. Ishihara, "Undrained Deformation Characteristics of Sand in Multi-Directional Shear," *Soils and Foundations* 23, no. 1 (1983): 61–79.

23. D. Su and X. Li, "Impact of Multidirectional Shaking on Liquefaction Potential of Level Sand Deposits," *Géotechnique* 58, no. 4 (2008): 259–267.

24. P. Gräbe and C. Clayton, "Effects of Principal Stress Rotation on permanent Deformation in Rail Track Foundations," *Journal of Geotechnical and Geoenvironmental Engineering, ASCE* 135, no. 4 (2009): 555–565.

25. H. Matsuda, A. P. Hendrawan, R. Ishikura, and S. Kawahara, "Effective Stress Change and Post-Earthquake Settlement Properties of Granular Materials Subjected to Multi-Directional Cyclic Simple Shear," *Soils and Foundations* 51, no. 5 (2011): 873–884.

26. A. Inam, T. Ishikawa, and S. Miura, "Effect of Principal Stress Axis Rotation on Cyclic Plastic Deformation Characteristics of Unsaturated Base Course Material," *Soils and Foundations* 52, no. 3 (2012): 465–480.

27. S. Sivathayalan, P. Logeswaran, and V. Manmatharajan, "Cyclic Resistance of a Loose Sand Subjected to Rotation of Principal Stresses," *Journal of Geotechnical and Geoenvironmental Engineering* 141 (2015): 04014113.

28. M. Yang, M. Taiebat, P. Mutabaruka, and F. Radjai, "Evolution of Granular Media Under Constant-Volume Multidirectional Cyclic Shearing," *Acta Geotechnica* 17, no. 3 (2022): 779–802.

29. A. Niemunis, T. Wichtmann, and T. Triantafyllidis, "A High-Cycle Accumulation Model for Sand," *Computers and Geotechnics* 32, no. 4 (2005): 245–263.

30. H. Zachert, T. Wichtmann, P. Kudella, and T. Triantafyllidis, "Inspection of a High-Cycle Accumulation Model for Sand Based on Recalculations of a Full-Scale Test on a Gravity Base Foundation for Offshore Wind Turbines," *Computers and Geotechnics* 126 (2020): 103727, https://doi.org/10.1016/j.compgeo.2020.103727.

31. M. Birrell, C. Pastén, J. A. Abell, and R. Astroza, "Probabilistic Characterization of a High-Cycle Accumulation Model for Sands," *Computers and Geotechnics* 147 (2022): 104798, https://doi.org/10.1016/j.compgeo.2022.104798.

32. A. M. Page, R. T. Klinkvort, S. Bayton, Y. Zhang, and H. P. Jostad, "A Procedure for Predicting the Permanent Rotation of Monopiles in Sand Supporting Offshore Wind Turbines," *Marine Structures* 75 (Jan 2021): 102813, https://doi.org/10.1016/j.marstruc.2020.102813.

33. H. P. Jostad, B. M. Dahl, A. Page, N. Sivasithamparam, and H. Sturm, "Evaluation of Soil Models for Improved Design of Offshore Wind Turbine Foundations in Dense Sand," *Geotechnique* 70, no. 8 (2020): 682–699, https://doi.org/10.1680/jgeot.19.TI.034.

34. P. Staubach and T. Wichtmann, "Long-Term Deformations of Monopile Foundations for Offshore Wind Turbines Studied With a High-Cycle Accumulation Model," *Computers and Geotechnics* 124, no. 8 (2020): 103553.

35. T. Wichtmann, "Soil Behaviour Under Cyclic Loading - Experimental Observations, Constitutive Description and Applications" (Habilitation Thesis, Publications of the Institute of Soil Mechanics and Rock Mechanics, Karlsruhe Institute of Technology, 2016). Issue No. 181.

36. L. Knittel, "Granular Soils Under Multidimensional Cyclic Loading" (diss., Institute for Soil Mechanics and Rock Mechanics, Karlsruhe Institute of Technology (KIT), 2020). No. 188.

37. T. Wichtmann, "Explicit Accumulation Model for Non-Cohesive Soils Under Cyclic Loading" (PhD thesis, Publications of the Institute of Soil Mechanics and Foundation Engineering, Ruhr-University Bochum, 2005). Issue No. 38.

38. A. Niemunis, "Extended Hypoplastic Models for Soils" (Habilitation, Veröffentlichungen des Institutes für Grundbau und Bodenmechanik, Ruhr-Universität Bochum, 2003). Heft Nr. 34.

39. P. Nicholson, R. Seed, and H. Anwar, "Elimination of Membrane Compliance in Undrained Triaxial Testing. I. Measurement and Evaluation," *Canadian Geotechnical Journal* 30, no. 5 (1993): 727–738.

40. K. Tokimatsu, "System Compliance Correction From Pore Pressure Response in Undrained Triaxial Tests," *Soils and Foundations* 30, no. 2 (1990): 14–22.

41. A. Niemunis and L. Knittel, "Removal of the Membrane Penetration Error From Triaxial Data," *Open Geomechanics* 2, no. 5 (2020): 13, https://doi.org/10.5802/ogeo.7

42. L. Knittel, T. Wichtmann, A. Niemunis, G. Huber, E. Espino, and T. Triantafyllidis, "Pure Elastic Stiffness of Sand Represented by Response Envelopes Derived From Cyclic Triaxial Tests With Local Strain Measurements," *Acta Geotechnica* 15, no. 8 (2020): 2075–2088, https://doi.org/10.1007/s11440-019-00893-9.

43. L. Knittel, A. Lamparter, A. Niemunis, and H. Stutz, "The High-Cyclic Model for Sand Tested Beyond the Usual Ranges of Application," *Acta Geotechnica* 19, no. 2 (2024): 549–560, https://doi.org/10.1007/s11440-023-02031-y

44. L. Knittel and M. Tafili, "State-Dependent Dilatancy of Sand Based on Hollow Cylinder Laboratory Tests Under Shear Strain Cycles," in *8th International Symposium on Deformation Characteristics of Geomaterials (ISDCG2023)* (Porto, Portugal: 2023), https://doi.org/10.1051/e3sconf/202454406002

45. T. Wichtmann and L. Knittel, "Behaviour of Granular Soils Under Uni- and Multidimensional Drained High-Cyclic Loading," in *Recent Developments of Soil Mechanics and Geotechnics in Theory and Practice*, ed. T. Triantafyllidis (Cham, Switzerland: Springer, 2019), 136–165, https://doi.org/10.1007/978-3-030-28516-6_8

46. J. Dührkop and J. Grabe, "Monopilegründungen von Offshore-Windenergieanlagen - Zum Einfluss einer veränderlichen zyklischen Lastangriffsrichtung," *Bautechnik* 85, no. 5 (2008): 317–321.

47. C. Rudolph, B. Bienen, and J. Grabe, "Effect of Variation of the Loading Direction on the Displacement Accumulation of Large-Diameter Piles Under Cyclic Lateral Loading in Sand," *Canadian Geotechnical Journal* 51, no. 10 (2014): 1196–1206.

48. C. Leblanc, G. Houlsby, and B. Byrne, "Response of Stiff Piles in Sand to Long-Term Cyclic Lateral Loading," *Géotechnique* 60, no. 2 (2010): 79–90.

49. P. Staubach, J. Machaček, M. C. Moscoso, and T. Wichtmann, "Impact of the Installation on the Long-Term Cyclic Behaviour of Piles in Sand: A Numerical Study," *Soil Dynamics and Earthquake Engineering* 138 (2020): 106223, https://doi.org/10.1016/j.soildyn.2020.106223.

50. P. Staubach, J. Machaček, R. Sharif, and T. Wichtmann, "Back-Analysis of Model Tests on Piles in Sand Subjected to Long-Term Lateral Cyclic Loading: Impact of the Pile Installation and Application of the HCA Model," *Computers and Geotechnics* 134 (June 2021): 104018, https://doi.org/10.1016/j.compgeo.2021.104018.

51. P. Staubach, J. Machaček, B. Bienen, and T. Wichtmann, "Long-Term Response of Piles to Cyclic Lateral Loading Following Vibratory and Impact Driving in Water-Saturated Sand," *Journal of Geotechnical and Geoenvironmental Engineering* 148, no. 11 (Nov 2022): 4022097, https://doi.org/10.1061/(ASCE)GT.1943-5606.0002906.

52. S. Fan, B. Bienen, and M. F. Randolph, "Effects of Monopile Installation on Subsequent Lateral Response in Sand. II: Lateral Loading," *Journal of Geotechnical and Geoenvironmental Engineering* 147, no. 5 (May 2021): 04021022, https://doi.org/10.1061/(ASCE)GT.1943-5606.0002504.

53. B. Bienen, S. Fan, M. Schröder, and M. F. Randolph, "Effect of the Installation Process on Monopile Lateral Response," *Proceedings of the Institution of Civil Engineers - Geotechnical Engineering* 174 (Sep 2021): 1–19, https://doi.org/10.1680/jgeen.20.00219.

54. P. Staubach, "Contributions to the Numerical Modelling of Pile Installation Processes and High-Cyclic Loading of Soils," (PhD thesis, Publications of the Chair of Soil Mechanics, Foundation Engineering and Environmental Geotechnics, Ruhr-University Bochum, 2022). Issue No. 73.

55. P.-A. von Wolffersdorff, "A Hypoplastic Relation for Granular Materials With a Predefined Limit State Surface," *Mechanics of Cohesive-Frictional Materials* 1, no. 3 (1996): 251–271.

56. A. Niemunis and I. Herle, "Hypoplastic Model for Cohesionless Soils With Elastic Strain Range," *Mechanics of Cohesive-Frictional Materials* 2, no. 4 (1997): 279–299.

57. I. A. Richards, M. F. Bransby, B. W. Byrne, C. Gaudin, and G. T. Houlsby, "Effect of Stress Level on Response of Model Monopile to Cyclic Lateral Loading in Sand," *Journal of Geotechnical and Geoenvironmental Engineering* 147, no. 3 (2021): 04021002, https://doi.org/10.1061/(ASCE)GT.1943-5606.0002447.

58. P. Staubach, J. Machaček, and T. Wichtmann, "Large-Deformation Analysis of Pile Installation With Subsequent Lateral Loading: Sanisand vs. Hypoplasticity," *Soil Dynamics and Earthquake Engineering* 151 (Dec 2021): 106964, https://doi.org/10.1016/j.soildyn.2021.106964.

59. J. Machaček, "Contributions to the Numerical Modelling of Saturated and Unsaturated Soils," (diss., Publications of the Institute of Soil Mechanics and Rock Mechanics, Karlsruhe Institute of Technology, 2020). Issue No. 187.

60. J. Machaček, P. Staubach, M. Tafili, H. Zachert, and T. Wichtmann, "Investigation of Three Sophisticated Constitutive Soil Models: From Numerical Formulations to Element Tests and the Analysis of Vibratory Pile Driving Tests," *Computers and Geotechnics* 138 (Oct 2021): 104276, https://doi.org/10.1016/j.compgeo.2021.104276.

61. P. Staubach, J. Machaček, and T. Wichtmann, "Mortar Contact Discretisation Methods Incorporating Interface Models Based on Hypoplasticity and Sanisand: Application to Vibratory Pile Driving," *Computers and Geotechnics* 146 (June 2022): 104677, https://doi.org/10.1016/j.compgeo.2022.104677.

62. E. Heins and J. Grabe, "Class-A-Prediction of Lateral Pile Deformation With Respect to Vibratory and Impact Pile Driving," *Computers and Geotechnics* 86 (2017): 108–119, https://doi.org/10.1016/j.compgeo.2017.01.007.

63. H. Liu, E. Kementzetzidis, J. A. Abell, and F. Pisanò, "From Cyclic Sand Ratcheting to Tilt Accumulation of Offshore Monopiles: 3D FE Modelling Using SANISAND-MS," *Géotechnique* 72, (2021): 1–16, https://doi.org/10.1680/jgeot.20.p.029.

Appendix A: Detailed Testing Program

For the 1D stress paths, Table A.1 specifies the tested spans (lengths, double amplitudes) l_{PQ} and the inclinations (polarizations) α_{PQ} in the P–Q plane. A polarization $\alpha_{PQ} = 54.75°$ indicates a conventional cyclic axial loading at constant lateral effective stress. The dots in the table signify that spans ranging from $l_{PQ} = 40$ kPa to $l_{PQ} = 200$ kPa were tested in increments of $\Delta l_{PQ} = 10$ kPa. For 2D stress paths, the spans a_{PQ} and b_{PQ} along two orthogonal axes and the orientation α_{PQ} of the longer axis are provided in Table A.2. For circular 2D stress paths, the condition $a_{PQ} = b_{PQ} = r_{PQ}$ applies. A polarization α_{PQ} cannot be defined for circular paths. The program of the tests in the hollow cylinder device is shown in Table 1. The first test serves as a reference test. It was conducted in analogy to the circular 2D stress paths used in the cyclic triaxial tests, with a radius $r_{PQ} = 40$ kPa in the P–Q plane. This stress loop is achieved through cyclic variations of the vertical and radial stresses, with amplitudes of $\sigma_z^{ampl} = 40$ kPa and $\sigma_r^{ampl} = 28.28$ kPa. These amplitudes were kept constant throughout the entire test series. By cyclically varying

TABLE A.1 | Cyclic triaxial test program with 1D stress paths. The components α_{PQ} and l_{PQ} are exemplary illustrated in Figure B.1a.

Dimension	Polarization $\alpha_{PQ}[°]$	Span $l_{PQ}[kPa]$
1D	54.75	40.00
1D	54.75	50.00
1D	54.75	—
1D	54.75	190.00
1D	54.75	200.00
1D	0	80.00
1D	45	80.00
1D	90	80.00
1D	135	80.00
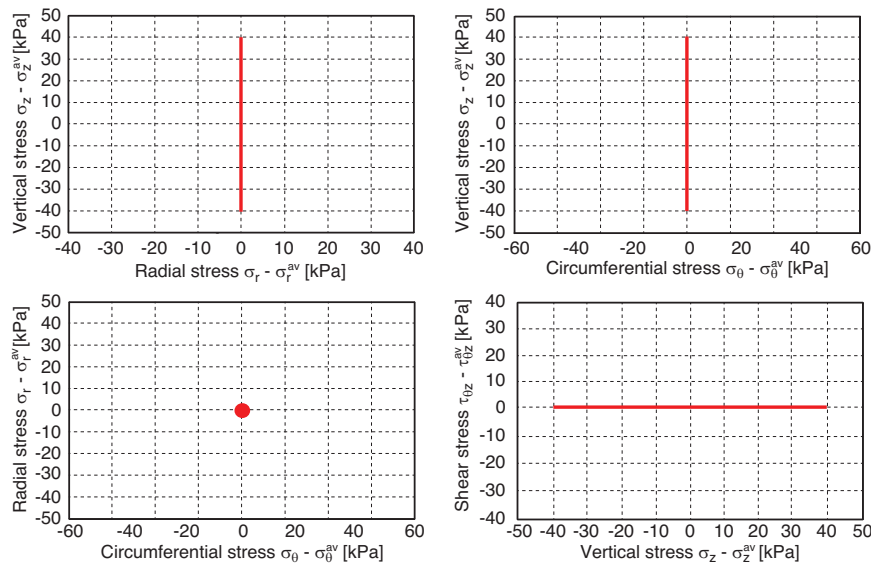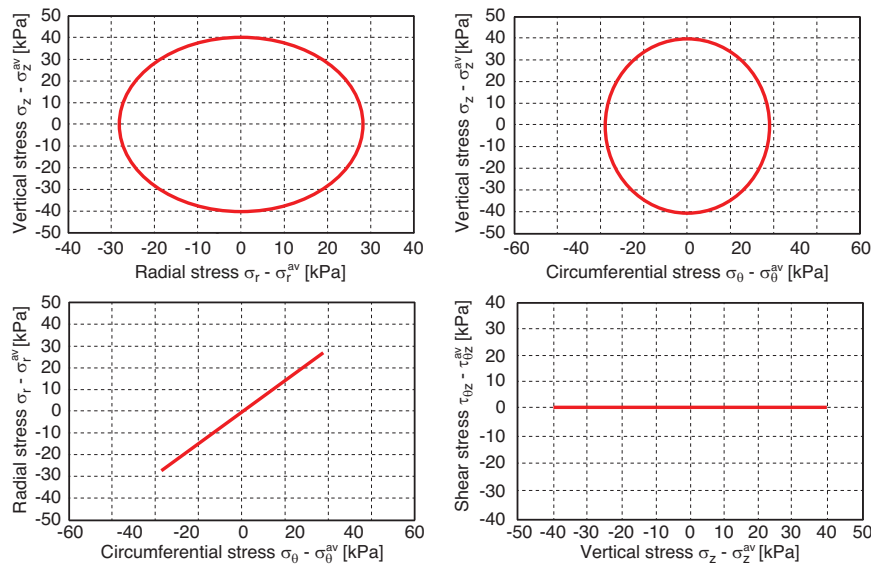
FIGURE A.1 | Plots of the prescribed stress paths in σ_z–σ_r–σ_θ–$\tau_{\theta z}$ diagrams for (a) one-dimensional loading with $\sigma_z^{ampl} = 40$ kPa (see Table A.1) and (b) two-dimensional loading (No. 1, Table A.2).
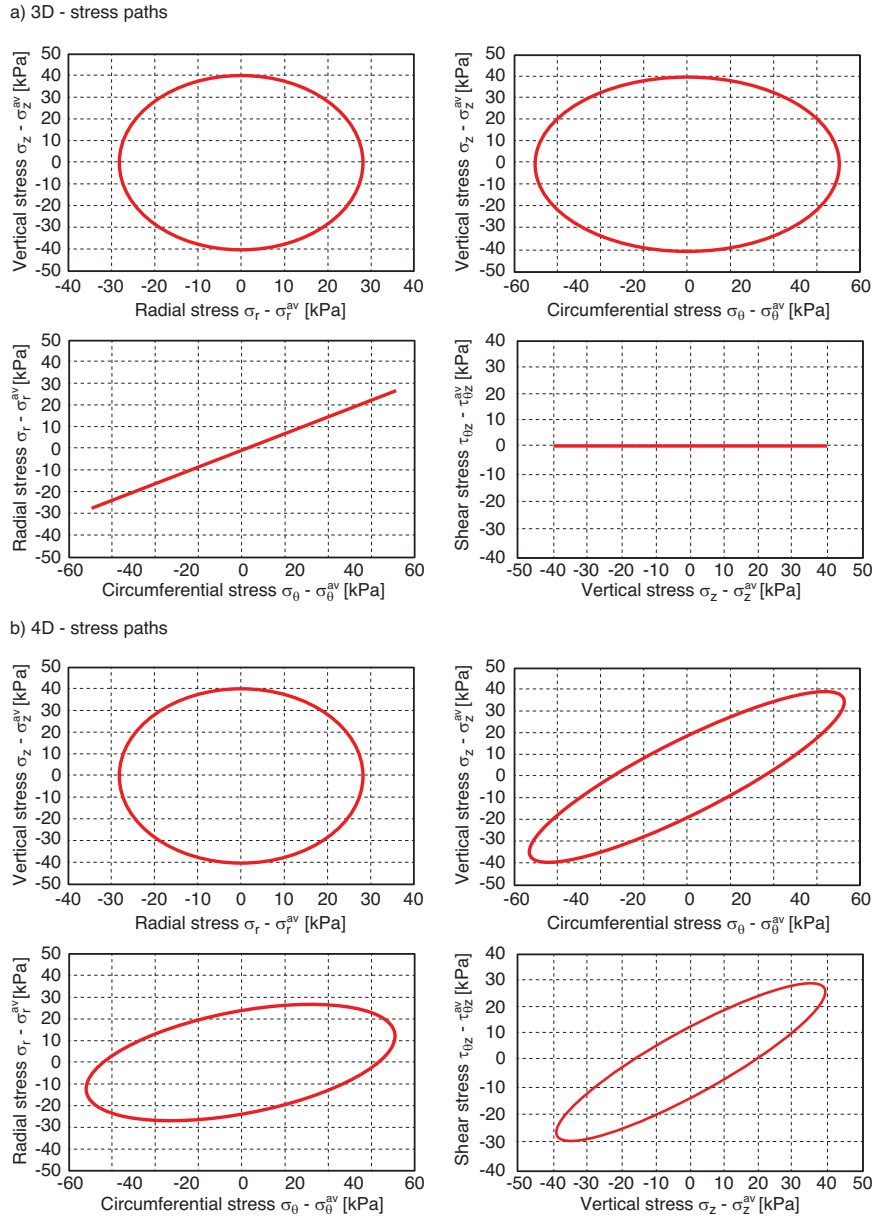
International Journal for Numerical and Analytical Methods in Geomechanics, 2025

a) 3D - stress paths

b) 4D - stress paths

FIGURE A.2 | Plots of the prescribed stress paths in σ_z–σ_r–σ_θ–$\tau_{\theta z}$ diagrams for (a) three-dimensional loading (No. 2, Table 1) and (b) four-dimensional loading (No. 4, Table 1).

TABLE A.2 | Cyclic triaxial test program with 2D stress paths. The components α_{PQ}, a_{PQ}, and b_{PQ} are exemplary illustrated in Figure B.1a.

Dimension	Polarization $\alpha_{PQ}[°]$	Span a_{PQ}[kPa]	Span b_{PQ}[kPa]
2D	—	28.28	28.28
2D	—	40.00	40.00
2D	—	60.00	60.00
2D	—	80.00	80.00
2D	0	35.78	17.78
2D	0	80.00	40.00
2D	45	80.00	40.00
2D	90	80.00	40.00
2D	135	80.00	40.00

the remaining two stress components, σ_θ and $\tau_{\theta z}$, with amplitudes $\sigma_\theta^{\mathrm{ampl}}$ and $\tau_{\theta z}^{\mathrm{ampl}}$, and by selecting different phase shift values ϕ between the various stress components, up to 4D stress paths could be explored. The loading frequency was the same for all four stress components.

A visual representation of the applied stress paths for selected tests in multidimensional stress space is shown in Figures A.1 and A.2. Figure A.1a illustrates a one-dimensional load where the vertical stress oscillates with an amplitude of $\sigma_z^{\mathrm{ampl}} = 40$ kPa (Table A.1), while radial and circumferential stresses remain constant. This exclusive variation of vertical stress leads to a polarization angle of $\alpha_{PQ} = 54.75°$ in the P–Q space. Two-dimensional stress paths from a triaxial test and a hollow cylinder test (Table A.2) are shown in Figure A.1b, where both the outer and inner cell pressures are varied cyclically with equal amplitude, while torsional shear stress $\tau_{\theta z}$ remains zero. Figure A.2a depicts the three-dimensional stress loop (No. 2, Table 1) from a hollow cylinder test, where the radial, circumferential, and vertical stresses are cyclically varied, with $\tau_{\theta z}$ kept at zero. A four-dimensional stress loop, shown in Figure A.2b (No.
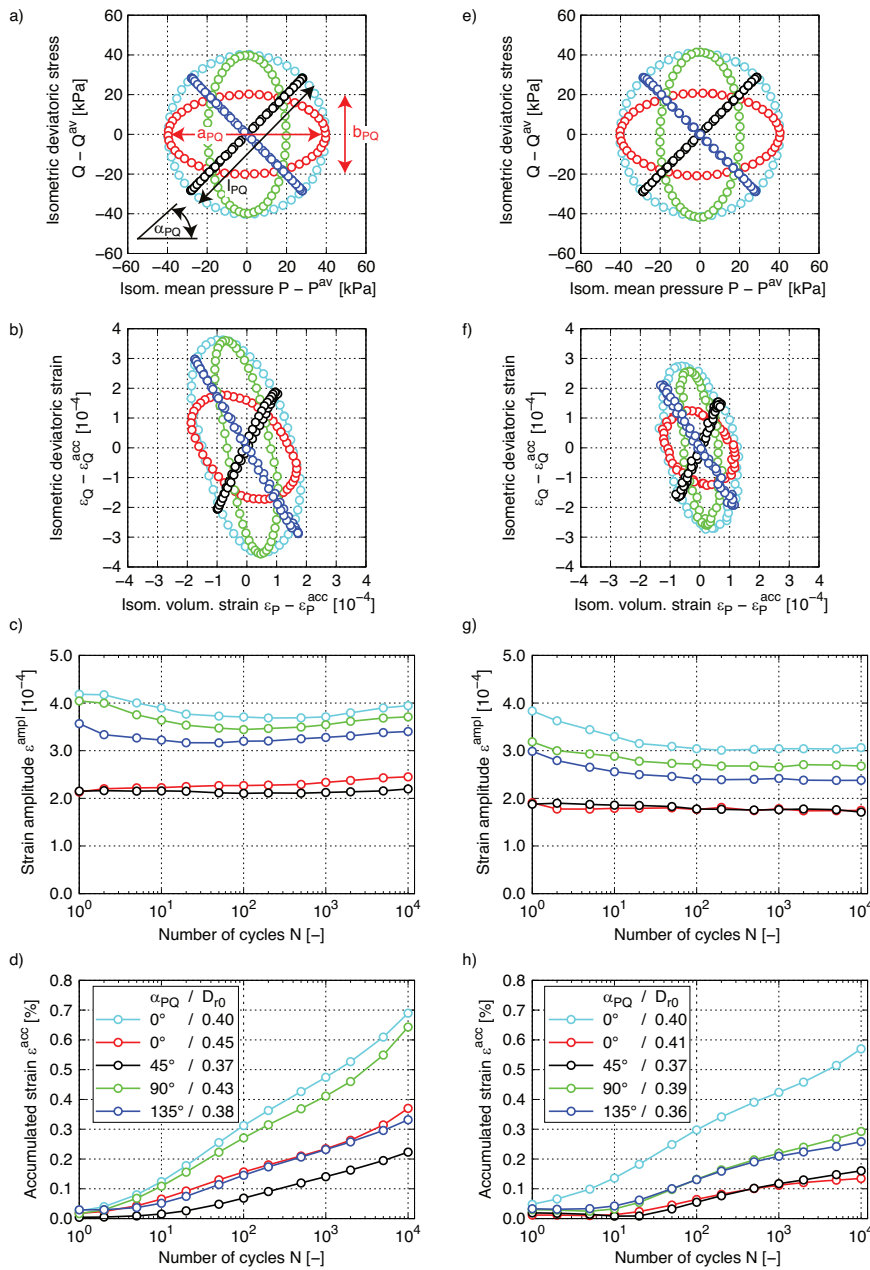
FIGURE B.1 | Selected cyclic triaxial tests on fully water-saturated full cylinder samples (left-hand side) and dry cuboid-shaped samples (right-hand side): (a, e) P–Q stress paths, (b, f) ε_P–ε_Q strain paths at $N = 10{,}000$, (c, g) development of strain amplitude $\varepsilon^{\mathrm{ampl}}$, and (d, h) accumulated strain $\varepsilon^{\mathrm{acc}}$ with increasing number of cycles N in tests on medium dense samples ($D_{r0} \approx 40\%$).

4, Table 1), involves cyclic variations of external and internal pressures, vertical stress, and torsional stress, leading to the emergence of shear strains $\gamma_{\theta z}$.

Appendix B: Water-Saturated Cylindrical Samples Versus Dry Cuboid-Shaped Samples With Local Strain Measurements

Figure B.1 compares data from triaxial tests on fully water-saturated cylindrical samples (with global strain measurements, left) and dry cuboid samples (with local strain measurements, right). Results are shown for two 1D stress paths with inclinations α_{PQ} of $-45°$ and $45°$, two elliptical 2D paths with inclinations of $\alpha_{PQ} = 0°$ and $90°$, and a circular 2D path. The first and second rows of Figure B.1 show that circular stress paths

in the P–Q plane produce elliptical strain paths in the ε_P–ε_Q plane, with a longer axis in the deviatoric direction. Strain amplitudes, calculated as described by Niemunis [38] and illustrated in Figure 3, increase with the area enclosed by the strain path. The smallest strain amplitudes are for the 1D path with $\alpha_{PQ} = 45°$, and the largest are for the circular 2D path. Notably, strain amplitudes from local measurements on dry samples (Figure B.1g) are slightly lower than those from global measurements on saturated samples (Figure B.1c), likely due to saturation differences rather than measurement methods or sample geometry. The higher stiffness of KFS in the dry condition compared to the water-saturated state has been already observed in previous experimental studies, using cylindrical samples and global measurements in all tests [35]. As shown in Figure B.1c,d,g,h, higher strain amplitudes result in larger cumulative strains for both sample types and saturation conditions.